Master's thesis of engineering

Diffractive optics for augmented reality display

Improvement in the field of view and eye box

증강현실 디스플레이를 위한 회절 광학

August 2023

Graduate School of Engineering
Seoul National University
Electrical and Computer Engineering

Jee Hyun Lee

Diffractive optics for augmented reality display

Improvement in the field of view and eye box

Supervisor Jongmo Seo

Submitting a master's thesis of engineering

August 2023

Graduate School of Engineering
Seoul National University
Electrical and Computer Engineering

Confirming the master's thesis written by

Jee Hyun Lee

August 2023

Chair	Jae-Sang Lee	(Seal)
Vice Chair	Jongmo Seo	(Seal)
Examiner	Jae-Hyeung Park	(Seal)

Abstract

Augmented reality near eye display systems aim to enhance real world experience by superimposing virtual images and projecting these to the human eye. This field has garnered interest over the years, with increasing demand for a head-mounted device that provides a truly immersive experience of metaverse. However, despite the advancements, various challenges remain.

Development of AR NED systems suffer from a range of issues, including conventional display-related issues such as luminance and pixel quality as well as problems comparatively unique to near-eye display. Field of view and eye box would be examples of the latter, having gained significance due to the proximity of the eye and the display.

In this dissertation, the primary objective is to attempt to address challenges related to the field of view and eye box in AR NED systems. Geometric-optics based ray tracing and k-vector analysis, along with Fourier modal method are employed in the design and validation of the presented waveguide models. For the expansion of the field of view, a dual expander waveguide combiner is presented. The eye box issue is addressed with a waveguide model that integrates the expander and output coupler by utilizing overlaid gratings or rhombus-shaped gratings. With the objective of attaining uniform light outcoupling from the integrated outcoupler, genetic algorithm and an additional post-processing step are employed for optimization of the diffraction efficiency.

Keyword : augmented reality, diffractive optics, near-eye display, head-mounted display, ray-tracing, Fourier modal method
Student Number : 2021-20673

Table of Contents

Chapter 1. Introduction

1.1. Purpose of research

In recent years, *metaverse* has become a key term for a budding industrial sector that aims to create digital worlds allowing real-time interaction. Currently, this concept has been primarily realized on conventional 2D platforms accessible via phone, tablet, or PC. For instance, during the COVID-19 pandemic when physical interactions were restricted, such platforms were used to host events such as commencement ceremonies and other various activities. Other examples include 2D mobile applications such as Zepeto that allow users to engage with each other within a digital world as virtual avatars.

Nonetheless, the ultimate objective of metaverse realization would be to provide genuinely immersive, three-dimensional user experience that goes beyond traditional 2D implementations. With this overarching aim, the next logical step is to develop near-eye display (NED) technologies that span from virtual reality(VR) to augmented reality(AR)applications. On the one hand, virtual reality(VR) devices aim to solely provide digitally synthesized video content without visual information on the real-world surroundings of the user. The goal for augmented reality (AR) devices, on the other hand, is to enrich real-world experiences by superimposing virtual elements on top of the visual information of the user's true surroundings.

Current NED devices, both for AR and VR, however, exhibit limitations that must be addressed to enhance the user experience. These issues encompass both traditional display related problems as well as challenges arising from the proximity of the display and the human eye. Field of view, eye box, and form factor are examples of factors that are significant due to the distinctive property of NED devices[1,2].

In regards to FOV, AR devices suffer from stricter restraints in comparison to VR because of requirements for the proper performance of the optical combiner, an element that overlays the real and virtual world imagery. Other additional issues for AR

include luminance. This is a prominent problem for AR devices, since the computer-generated images must compete with real-world elements that possess a wide dynamic range in terms of brightness.

A near eye display system that offers clear images would be invaluable in revolutionizing the quality of engagement and interaction within metaverse platforms. This dissertation endeavors to investigate the optical combiner, the optical element that permits both the real and virtual image to be delivered to the eye and differentiates AR from VR, in hopes of presenting methods by which the field of view and eye box can be enlarged. The scope of the discussion will be limited to diffractive optics, with its strength in form factor when compared to a refractive optics approach.

Chapter 2. Analysis of Electromagnetic Fields

Chapter Overview

The primary focus of this chapter is to explain the Fourier modal method (FMM), the main technique employed in this dissertation to analyze electromagnetic fields. As the basis of modal analysis lies in the concept of electromagnetic eigenmodes, this chapter will provide an overview of Bloch eigenmodes and include a demonstration of a scattering matrix analysis applied to a single block structure. The Fourier modal method is an extension of the scattering matrix analysis for structures whose permittivity and permeability parameters vary in 2D and 3D[3].

2.1. Eigenmodes

Modal analysis exploits the fact that linear optical structures possess eigenmodes. These eigenmodes, when appropriately added with adequate coupling coefficients, can express any possible optical field within the structure.

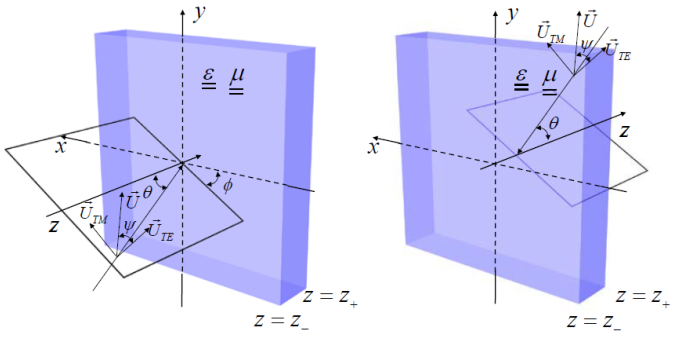

Fig. 2.1. A diagram of a single block structure

The eigenmodes of a single block structure whose permeability and permittivity profiles vary in only one dimension will be calculated as follows. The Bloch eigenmodes is derived from Maxwell's equations. The permittivity and permeability tensors are denoted by $\underline{\underline{\mu}}$ and $\underline{\underline{\varepsilon}}$, respectively. The angular frequency of the optical wave is denoted by ω.

(2.1) $$\nabla \times \mathbf{E} = j\omega\mu_0 \underline{\underline{\mu}}\mathbf{H}$$

(2.2) $$\nabla \times \mathbf{H} = -j\omega\varepsilon_0 \underline{\underline{\varepsilon}}\mathbf{E}$$

(2.3) $$\nabla \cdot (\underline{\underline{\varepsilon}}\mathbf{E}) = 0$$

(2.4) $$\nabla \cdot (\underline{\underline{\mu}}\mathbf{H}) = 0$$

For uniaxial or biaxial materials, the permittivity and permeability tensors can be expressed as below.

(2.5) $$\underline{\underline{\varepsilon}} = \begin{bmatrix} \varepsilon_{(x)} & 0 & 0 \\ 0 & \varepsilon_{(y)} & 0 \\ 0 & 0 & \varepsilon_{(z)} \end{bmatrix}$$

(2.6) $$\underline{\underline{\mu}} = \begin{bmatrix} \mu_{(x)} & 0 & 0 \\ 0 & \mu_{(y)} & 0 \\ 0 & 0 & \mu_{(z)} \end{bmatrix}$$

The electromagnetic fields of an eigenmode in homogeneous medium can be represented in the following plane wave form, where a scale factor of $j\sqrt{\varepsilon_0 / \mu_0}$ is included for ease of calculation. The wave vector is denoted by $\mathbf{k} = (k_x, k_y, k_z)$, where the z coordinate lies perpendicular to the surface of the single block.

(2.7) $$\mathbf{E} = (\mathbf{E}_x, \mathbf{E}_y, \mathbf{E}_z) = (E_x, E_y, E_z)e^{j(k_x x + k_y y + k_z z)}$$

(2.8) $$\mathbf{H} = (\mathbf{H}_x, \mathbf{H}_y, \mathbf{H}_z) = j\sqrt{\frac{\varepsilon_0}{\mu_0}}(H_x, H_y, H_z)e^{j(k_x x + k_y y + k_z z)}$$

With this formulation, the curl equations of 2.1 and 2.2 can be expressed as follows for an isotropic permittivity and permeability profile. The free space wave number is denoted by k_0.

(2.9)

$$k_0\begin{bmatrix}\varepsilon & 0 & 0 & 0 & 0 & 0\\ 0 & \varepsilon & 0 & 0 & 0 & 0\\ 0 & 0 & \varepsilon & 0 & 0 & 0\\ 0 & 0 & 0 & \mu & 0 & 0\\ 0 & 0 & 0 & 0 & \mu & 0\\ 0 & 0 & 0 & 0 & 0 & \mu\end{bmatrix}\begin{bmatrix}E_x\\ E_y\\ E_z\\ H_x\\ H_y\\ H_z\end{bmatrix}=\begin{bmatrix}0 & 0 & 0 & 0 & jk_z & -jk_y\\ 0 & 0 & 0 & -jk_z & 0 & jk_x\\ 0 & 0 & 0 & jk_y & -jk_x & 0\\ 0 & jk_z & -jk_y & 0 & 0 & 0\\ -jk_z & 0 & jk_x & 0 & 0 & 0\\ jk_y & -jk_x & 0 & 0 & 0 & 0\end{bmatrix}\begin{bmatrix}E_x\\ E_y\\ E_z\\ H_x\\ H_y\\ H_z\end{bmatrix}$$

The above equation can be generalized for structures with anisotropic permittivity and permeability.

$$k_0\begin{bmatrix}\varepsilon_x & 0 & 0 & 0 & 0 & 0\\ 0 & \varepsilon_y & 0 & 0 & 0 & 0\\ 0 & 0 & \varepsilon_z & 0 & 0 & 0\\ 0 & 0 & 0 & \mu_x & 0 & 0\\ 0 & 0 & 0 & 0 & \mu_y & 0\\ 0 & 0 & 0 & 0 & 0 & \mu_z\end{bmatrix}\begin{bmatrix}E_x\\ E_y\\ E_z\\ H_x\\ H_y\\ H_z\end{bmatrix}$$

(2.10)

$$=\begin{bmatrix}0 & 0 & 0 & 0 & jk_z & -jk_y\\ 0 & 0 & 0 & -jk_z & 0 & jk_x\\ 0 & 0 & 0 & jk_y & -jk_x & 0\\ 0 & jk_z & -jk_y & 0 & 0 & 0\\ -jk_z & 0 & jk_x & 0 & 0 & 0\\ jk_y & -jk_x & 0 & 0 & 0 & 0\end{bmatrix}\begin{bmatrix}E_x\\ E_y\\ E_z\\ H_x\\ H_y\\ H_z\end{bmatrix}$$

The matrix form of the equation 2.10 explicitly shows that this is a matrix eigenvalue equation. To attain the dispersion relation, the above 6x6 matrix equation can be divided into two separate 3x3 matrix equations. When one is plugged into the other, the resultant equation is as below.

$$\begin{bmatrix}\varepsilon_x^{-1} & 0 & 0\\ 0 & \varepsilon_y^{-1} & 0\\ 0 & 0 & \varepsilon_z^{-1}\end{bmatrix}\begin{bmatrix}0 & jk_z & -jk_y\\ -jk_z & 0 & jk_x\\ jk_y & -jk_x & 0\end{bmatrix}$$

(2.11)

$$\times\begin{bmatrix}\mu_x^{-1} & 0 & 0\\ 0 & \mu_y^{-1} & 0\\ 0 & 0 & \mu_z^{-1}\end{bmatrix}\begin{bmatrix}0 & jk_z & -jk_y\\ -jk_z & 0 & jk_x\\ jk_y & -jk_x & 0\end{bmatrix}\begin{bmatrix}E_x\\ E_y\\ E_z\end{bmatrix}=\left(\frac{\omega}{c}\right)^2\begin{bmatrix}E_x\\ E_y\\ E_z\end{bmatrix}$$

A simple calculation shows that the below equation is equivalent to 2.11.

(2.12)

$$\begin{bmatrix} \left(\frac{\omega}{c}\right)^2 - \left(\frac{k_y^{\ 2}}{\mu_z\varepsilon_x} + \frac{k_z^{\ 2}}{\mu_y\varepsilon_x}\right) & \frac{k_x k_y}{\varepsilon_x\mu_z} & \frac{k_z k_x}{\varepsilon_x\mu_y} \\ \frac{k_x k_y}{\varepsilon_y\mu_z} & \left(\frac{\omega}{c}\right)^2 - \left(\frac{k_z^{\ 2}}{\mu_x\varepsilon_y} + \frac{k_x^{\ 2}}{\mu_z\varepsilon_y}\right) & \frac{k_y k_z}{\varepsilon_y\mu_x} \\ \frac{k_z k_x}{\varepsilon_z\mu_y} & \frac{k_y k_z}{\varepsilon_z\mu_x} & \left(\frac{\omega}{c}\right)^2 - \left(\frac{k_x^{\ 2}}{\mu_y\varepsilon_z} + \frac{k_y^{\ 2}}{\mu_x\varepsilon_z}\right) \end{bmatrix} \begin{bmatrix} E_x \\ E_y \\ E_z \end{bmatrix} = \begin{bmatrix} 0 \\ 0 \\ 0 \end{bmatrix}$$

The eigenvalue can be acquired by solving for the condition of zero determinant for the above equation. For homogeneous media, this can be achieved analytically, leading to the dispersion relation Eq. 2.14.

(2.13)

$$\left[\left(\frac{\omega}{c}\right)^2\right]^2 - \left\{k_x^{\ 2}\left(\frac{1}{\varepsilon_y\mu_z} + \frac{1}{\mu_y\varepsilon_z}\right) + k_y^{\ 2}\left(\frac{1}{\varepsilon_z\mu_x} + \frac{1}{\mu_z\varepsilon_x}\right) + k_z^{\ 2}\left(\frac{1}{\varepsilon_x\mu_y} + \frac{1}{\mu_x\varepsilon_y}\right)\right\}\left(\frac{\omega}{c}\right)^2$$
$$+ \left\{\begin{array}{l} \frac{k_x^{\ 4}}{\varepsilon_y\mu_z\mu_y\varepsilon_z} + \frac{k_y^{\ 4}}{\varepsilon_z\mu_x\mu_z\varepsilon_x} + \frac{k_z^{\ 4}}{\varepsilon_x\mu_y\mu_x\varepsilon_y} \\ + \frac{k_x^{\ 2}k_y^{\ 2}}{\varepsilon_z\mu_z}\left(\frac{1}{\varepsilon_x\mu_y} + \frac{1}{\mu_x\varepsilon_y}\right) + \frac{k_y^{\ 2}k_z^{\ 2}}{\varepsilon_x\mu_x}\left(\frac{1}{\varepsilon_y\mu_z} + \frac{1}{\mu_y\varepsilon_z}\right) + \frac{k_x^{\ 2}k_x^{\ 2}}{\varepsilon_y\mu_y}\left(\frac{1}{\varepsilon_z\mu_x} + \frac{1}{\mu_z\varepsilon_x}\right) \end{array}\right\} = 0$$

(2.14) $$\left(\frac{\omega}{c}\right)^2 = \frac{1}{2}\left[(X+Y+Z) \pm \sqrt{X'^2 + Y'^2 + Z'^2 - 2(X'Y' + Y'Z' + Z'X')}\right]$$

$X, Y, Z, X', Y',$ and Z' are given, as follows.

$$X = k_x^{\ 2}\left(\frac{1}{\varepsilon_y\mu_z} + \frac{1}{\mu_y\varepsilon_z}\right), Y = k_y^{\ 2}\left(\frac{1}{\varepsilon_z\mu_x} + \frac{1}{\mu_z\varepsilon_x}\right), Z = k_z^{\ 2}\left(\frac{1}{\varepsilon_x\mu_y} + \frac{1}{\mu_x\varepsilon_y}\right)$$

$$X' = k_x^{\ 2}\left(\frac{1}{\varepsilon_y\mu_z} - \frac{1}{\mu_y\varepsilon_z}\right), Y' = k_y^{\ 2}\left(\frac{1}{\varepsilon_z\mu_x} - \frac{1}{\mu_z\varepsilon_x}\right), Z' = k_z^{\ 2}\left(\frac{1}{\varepsilon_x\mu_y} - \frac{1}{\mu_x\varepsilon_y}\right)$$

The matrix equation Eq. 2.10 can be transformed as below.

(2.15) $$j(k_z / k_0)E_y = \mu_x H_x + j(k_y / k_0)E_z$$

(2.16) $$j(k_z / k_0)E_x = -\mu_y H_y + j(k_x / k_0)E_z$$

(2.17) $$H_z = \mu_z^{-1}[j(k_y / k_0)E_x - j(k_x / k_0)E_y]$$

(2.18) $$j(k_z / k_0)H_y = \varepsilon_x E_x + j(k_y / k_0)H_z$$

(2.19) $$j(k_z / k_0)H_x = -\varepsilon_y E_y + j(k_x / k_0)H_z$$

(2.20) $$E_z = \varepsilon_z^{-1}[j(k_y / k_0)H_x - j(k_x / k_0)H_y]$$

The above equations can be remanipulated and be expressed as the following, where $\overline{k}_x = k_x / k_0, \overline{k}_y = k_y / k_0$, and $\overline{k}_z = k_z / k_0$.

(2.21)

$$\begin{bmatrix} 0 & 0 & \overline{k}_y \varepsilon_z^{-1} \overline{k}_x & \mu_x - \overline{k}_y \varepsilon_z^{-1} \overline{k}_y \\ 0 & 0 & -\mu_y + \overline{k}_x \varepsilon_z^{-1} \overline{k}_x & -\overline{k}_x \varepsilon_z^{-1} \overline{k}_y \\ \overline{k}_y \mu_z^{-1} \overline{k}_x & \varepsilon_x - \overline{k}_y \mu_z^{-1} \overline{k}_y & 0 & 0 \\ -\varepsilon_y + \overline{k}_x \mu_z^{-1} \overline{k}_x & -\overline{k}_x \mu_z^{-1} \overline{k}_y & 0 & 0 \end{bmatrix} \begin{bmatrix} E_y \\ E_x \\ H_y \\ H_x \end{bmatrix} = j\overline{k}_z \begin{bmatrix} E_y \\ E_x \\ H_y \\ H_x \end{bmatrix}$$

As the matrix dimension is four, there are four eigensolutions physically corresponding to right−to−left directional TE and TM modes and left−to−right directional TE and TM modes. Eq. 2.21 can be parted into two 2x2 matrix equations that can be again manipulated to lead to Eq. 2.22.

(2.22)

$$k_0^2 \begin{bmatrix} \overline{k}_y \varepsilon_z^{-1} \overline{k}_x & \mu_x - \overline{k}_y \varepsilon_z^{-1} \overline{k}_y \\ -\mu_y + \overline{k}_x \varepsilon_z^{-1} \overline{k}_x & -\overline{k}_x \varepsilon_z^{-1} \overline{k}_y \end{bmatrix} \begin{bmatrix} \overline{k}_y \mu_z^{-1} \overline{k}_x & \varepsilon_x - \overline{k}_y \mu_z^{-1} \overline{k}_y \\ -\varepsilon_y + \overline{k}_x \mu_z^{-1} \overline{k}_x & -\overline{k}_x \mu_z^{-1} \overline{k}_y \end{bmatrix} \begin{bmatrix} E_y \\ E_x \end{bmatrix} = (jk_z)^2 \begin{bmatrix} E_y \\ E_x \end{bmatrix}$$

(2.23) $$\begin{bmatrix} H_y \\ H_x \end{bmatrix} = j\overline{k}_z \begin{bmatrix} \overline{k}_y \varepsilon_z^{-1} \overline{k}_x & \mu_x - \overline{k}_y \varepsilon_z^{-1} \overline{k}_y \\ -\mu_y + \overline{k}_x \varepsilon_z^{-1} \overline{k}_x & -\overline{k}_x \varepsilon_z^{-1} \overline{k}_y \end{bmatrix}^{-1} \begin{bmatrix} E_y \\ E_x \end{bmatrix}$$

The z components of the electric and magnetic fields were given as below in Eq. 2.17 and Eq. 2.20.

(2.24) $$E_z = \varepsilon_z^{-1} \left[j(k_y / k_0) H_x - j(k_x / k_0) H_y \right]$$

(2.25) $$H_z = \mu_z^{-1} \left[j(k_y / k_0) E_x - j(k_x / k_0) E_y \right]$$

The above process can be applied to general anisotropic medium to acquire positive and negative modes. After renormalization of the magnetic field, the gth internal eigenmodes in the single−block are expressed in the Bloch wave form below.

(2.26) $$\begin{bmatrix} \mathbf{E}^{(g)} \\ \mathbf{H}^{(g)} \end{bmatrix} = \begin{bmatrix} \mathbf{E}_x^{(g)}, \mathbf{E}_y^{(g)}, \mathbf{E}_z^{(g)} \\ \mathbf{H}_x^{(g)}, \mathbf{H}_y^{(g)}, \mathbf{H}_z^{(g)} \end{bmatrix} = \begin{bmatrix} E_x^{(g)}, E_y^{(g)}, E_z^{(g)} \\ H_x^{(g)}, H_y^{(g)}, H_z^{(g)} \end{bmatrix} e^{j(k_x x + k_y y + k_z^{(g)} z)}$$

2.2. Scattering matrix analysis and Fourier Modal Method

Scattering matrix analysis adopts a matrix form to express the reflective and transmissive properties at an interface. From the curl equations of Maxwell's equations, the below equations for the tangential components of the incident, reflection, and transmission magnetic fields can be derived.

(2.27) $$\overrightarrow{\mathbf{H}}_{i,y} = \frac{1}{j\omega\mu_0}\left(\frac{\partial \overrightarrow{E}_{i,x}}{\partial z} - \frac{\partial \overrightarrow{E}_{i,z}}{\partial x}\right) \Leftrightarrow \overrightarrow{H}_{i,y} = \frac{1}{\omega\mu_0}(k_z \overrightarrow{E}_{i,x} - k_x \overrightarrow{E}_{i,z})$$

(2.28) $$\overrightarrow{\mathbf{H}}_{i,x} = \frac{1}{j\omega\mu_0}\left(\frac{\partial \overrightarrow{E}_{i,z}}{\partial y} - \frac{\partial \overrightarrow{E}_{i,y}}{\partial z}\right) \Leftrightarrow \overrightarrow{H}_{i,x} = \frac{1}{\omega\mu_0}(k_y \overrightarrow{E}_{i,z} - k_z \overrightarrow{E}_{i,y})$$

(2.29) $$\overrightarrow{\mathbf{H}}_{r,y} = \frac{1}{j\omega\mu_0}\left(\frac{\partial \overrightarrow{E}_{r,z}}{\partial z} - \frac{\partial \overrightarrow{E}_{r,y}}{\partial x}\right) \Leftrightarrow \overrightarrow{H}_{r,x} = \frac{1}{\omega\mu_0}(-k_z \overrightarrow{E}_{r,x} - k_x \overrightarrow{E}_{r,z})$$

(2.30) $$\overrightarrow{\mathbf{H}}_{r,x} = \frac{1}{j\omega\mu_0}\left(\frac{\partial \overrightarrow{E}_{r,z}}{\partial y} - \frac{\partial \overrightarrow{E}_{r,y}}{\partial z}\right) \Leftrightarrow \overrightarrow{H}_{r,x} = \frac{1}{\omega\mu_0}(k_y \overrightarrow{E}_{r,z} + k_z \overrightarrow{E}_{r,y})$$

(2.31) $$\overrightarrow{\mathbf{H}}_{t,y} = \frac{1}{j\omega\mu_0}\left(\frac{\partial \overrightarrow{E}_{t,x}}{\partial z} - \frac{\partial \overrightarrow{E}_{t,z}}{\partial x}\right) \Leftrightarrow \overrightarrow{H}_{t,y} = \frac{1}{\omega\mu_0}(k_z \overrightarrow{E}_{t,x} - k_x \overrightarrow{E}_{t,z})$$

(2.32) $$\overrightarrow{\mathbf{H}}_{t,x} = \frac{1}{j\omega\mu_0}\left(\frac{\partial \overrightarrow{E}_{t,z}}{\partial y} - \frac{\partial \overrightarrow{E}_{t,y}}{\partial z}\right) \Leftrightarrow \overrightarrow{H}_{t,x} = \frac{1}{\omega\mu_0}(k_y \overrightarrow{E}_{t,z} - k_z \overrightarrow{E}_{t,y})$$

The plane wave condition in free space leads to the following equations.

(2.33) $$k_x \overleftarrow{E}_{r,x} + k_y \overleftarrow{E}_{r,y} - k_z \overleftarrow{E}_{r,z} = 0 \Leftrightarrow \overleftarrow{E}_{r,z} = \frac{k_x \overleftarrow{E}_{r,x} + k_y \overleftarrow{E}_{r,y}}{k_z}$$

(2.34) $$k_x \overleftarrow{E}_{t,x} + k_y \overleftarrow{E}_{t,y} + k_z \overleftarrow{E}_{t,z} = 0 \Leftrightarrow \overleftarrow{E}_{t,z} = -\frac{k_x \overleftarrow{E}_{t,x} + k_y \overleftarrow{E}_{t,y}}{k_z}$$

(2.35) $$k_x \overleftarrow{E}_{i,x} + k_y \overleftarrow{E}_{i,y} + k_z \overleftarrow{E}_{i,z} = 0 \Leftrightarrow \overleftarrow{E}_{i,z} = -\frac{k_x \overleftarrow{E}_{i,x} + k_y \overleftarrow{E}_{i,y}}{k_z}$$

The z directional electric field components can be eliminated from

2.27−2.32 and with the tangential field continuation condition, the boundary condition at the left−boundary of z=z− can be expressed by the matrix equation given below.

(2.36)

$$\begin{bmatrix} I & 0 & I & 0 \\ 0 & I & 0 & I \\ \frac{1}{\omega\mu_0}\frac{k_x k_y}{k_z} & \frac{1}{\omega\mu_0}\frac{(k_z{}^2+k_x{}^2)}{k_z} & -\frac{1}{\omega\mu_0}\frac{k_x k_y}{k_z} & -\frac{1}{\omega\mu_0}\frac{(k_z{}^2+k_x{}^2)}{k_z} \\ -\frac{1}{\omega\mu_0}\frac{(k_z{}^2+k_x{}^2)}{k_z} & -\frac{1}{\omega\mu_0}\frac{k_x k_y}{k_z} & \frac{1}{\omega\mu_0}\frac{(k_z{}^2+k_x{}^2)}{k_z} & \frac{1}{\omega\mu_0}\frac{k_x k_y}{k_z} \end{bmatrix} \begin{bmatrix} \overline{E}_{i,y} \\ \overline{E}_{i,x} \\ \overline{E}_{r,y} \\ \overline{E}_{r,x} \end{bmatrix}$$

$$= \begin{bmatrix} E_y{}^{(1)+} & E_y{}^{(2)+} & E_y{}^{(1)-}e^{jk_z{}^{(1)-}(z_- - z_+)} & E_y{}^{(2)-}e^{jk_z{}^{(2)-}(z_- - z_+)} \\ E_x{}^{(1)+} & E_x{}^{(2)+} & E_x{}^{(1)-}e^{jk_z{}^{(1)-}(z_- - z_+)} & E_x{}^{(2)-}e^{jk_z{}^{(2)-}(z_- - z_+)} \\ H_y{}^{(1)+} & H_y{}^{(2)+} & H_y{}^{(1)-}e^{jk_z{}^{(1)-}(z_- - z_+)} & H_y{}^{(2)-}e^{jk_z{}^{(2)-}(z_- - z_+)} \\ H_x{}^{(1)+} & H_x{}^{(2)+} & H_x{}^{(1)-}e^{jk_z{}^{(1)-}(z_- - z_+)} & H_x{}^{(2)-}e^{jk_z{}^{(2)-}(z_- - z_+)} \end{bmatrix} \begin{bmatrix} C_{a,1}{}^{+} \\ C_{a,2}{}^{+} \\ C_{a,1}{}^{-} \\ C_{a,2}{}^{-} \end{bmatrix}$$

The boundary condition at the right boundary of z=z+ can be expressed as below.

(2.37)

$$\begin{bmatrix} E_y{}^{(1)+}e^{jk_z{}^{(1)+}(z_+ - z_-)} & E_y{}^{(2)+}e^{jk_z{}^{(2)+}(z_+ - z_-)} & E_y{}^{(1)-} & E_y{}^{(2)-} \\ E_x{}^{(1)+}e^{jk_z{}^{(1)+}(z_+ - z_-)} & E_x{}^{(2)+}e^{jk_z{}^{(2)+}(z_+ - z_-)} & E_x{}^{(1)-} & E_x{}^{(2)-} \\ H_y{}^{(1)+}e^{jk_z{}^{(1)+}(z_+ - z_-)} & H_y{}^{(2)+}e^{jk_z{}^{(2)+}(z_+ - z_-)} & H_y{}^{(1)-} & H_y{}^{(2)-} \\ H_x{}^{(1)+}e^{jk_z{}^{(1)+}(z_+ - z_-)} & H_x{}^{(2)+}e^{jk_z{}^{(2)+}(z_+ - z_-)} & H_x{}^{(1)-} & H_x{}^{(2)-} \end{bmatrix} \begin{bmatrix} C_{a,1}{}^{+} \\ C_{a,2}{}^{+} \\ C_{a,1}{}^{-} \\ C_{a,2}{}^{-} \end{bmatrix}$$

$$= \begin{bmatrix} I & 0 & I & 0 \\ 0 & I & 0 & I \\ \frac{1}{\omega\mu_0}\frac{k_x k_y}{k_z} & \frac{1}{\omega\mu_0}\frac{(k_z{}^2+k_x{}^2)}{k_z} & -\frac{1}{\omega\mu_0}\frac{k_x k_y}{k_z} & -\frac{1}{\omega\mu_0}\frac{(k_z{}^2+k_x{}^2)}{k_z} \\ -\frac{1}{\omega\mu_0}\frac{(k_y{}^2+k_z{}^2)}{k_z} & -\frac{1}{\omega\mu_0}\frac{k_y k_z}{k_z} & \frac{1}{\omega\mu_0}\frac{(k_y{}^2+k_z{}^2)}{k_z} & \frac{1}{\omega\mu_0}\frac{k_y k_z}{k_z} \end{bmatrix} \begin{bmatrix} \overline{E}_{i,y} \\ \overline{E}_{i,x} \\ \overline{E}_{r,y} \\ \overline{E}_{r,x} \end{bmatrix}$$

The above two equations are equivalent to the following equations.

(2.38)
$$\begin{bmatrix} \underline{\underline{W}}_h & \underline{\underline{W}}_h \\ \underline{\underline{V}}_h & -\underline{\underline{V}}_h \end{bmatrix} \begin{bmatrix} \underline{\vec{E}}_i \\ \underline{\vec{E}}_r \end{bmatrix} = \begin{bmatrix} \underline{\underline{W}}^+(0) & \underline{\underline{W}}^-(z_- - z_+) \\ \underline{\underline{V}}^+(0) & \underline{\underline{V}}^-(z_- - z_+) \end{bmatrix} \begin{bmatrix} \underline{C}_a^{\ +} \\ \underline{C}_a^{\ -} \end{bmatrix}$$

(2.39)
$$\begin{bmatrix} \underline{\underline{W}}_h & \underline{\underline{W}}_h \\ \underline{\underline{V}}_h & -\underline{\underline{V}}_h \end{bmatrix} \begin{bmatrix} \underline{\vec{E}}_t \\ \underline{0} \end{bmatrix} = \begin{bmatrix} \underline{\underline{W}}^+(z_+ - z_-) & \underline{\underline{W}}^-(0) \\ \underline{\underline{V}}^+(z_+ - z_-) & \underline{\underline{V}}^-(0) \end{bmatrix} \begin{bmatrix} \underline{C}_a^{\ +} \\ \underline{C}_a^{\ -} \end{bmatrix}$$

The newly introduced matrices in Eq. 2.38 and 2.39 are as defined in Eq. 2.40−2.45.

(2.40)
$$\underline{\underline{W}}_h = \begin{bmatrix} 1 & 0 \\ 0 & 1 \end{bmatrix}$$

(2.41)
$$\underline{\underline{V}}_h = \begin{bmatrix} \dfrac{1}{\omega\mu_0}\dfrac{k_x k_y}{k_z} & \dfrac{1}{\omega\mu_0}\dfrac{(k_z^{\ 2} + k_x^{\ 2})}{k_z} \\ -\dfrac{1}{\omega\mu_0}\dfrac{(k_y^{\ 2} + k_x^{\ 2})}{k_z} & \dfrac{1}{\omega\mu_0}\dfrac{k_x k_y}{k_z} \end{bmatrix}$$

The 4x2 matrices $\underline{\underline{W}}^+(z), \underline{\underline{V}}^+(z)$ denote the positive modes.

(2.42)
$$\underline{\underline{W}}^+(z) = \begin{bmatrix} E_y^{\ (1)+} e^{jk_z^{\ (1)+} z} & E_y^{\ (2)+} e^{jk_z^{\ (2)+} z} \\ E_x^{\ (1)+} e^{jk_z^{\ (1)+} z} & E_x^{\ (2)+} e^{jk_z^{\ (2)+} z} \end{bmatrix}$$

(2.43)
$$\underline{\underline{V}}^+(z) = \begin{bmatrix} H_y^{\ (1)+} e^{jk_z^{\ (1)+} z} & H_y^{\ (2)+} e^{jk_z^{\ (2)+} z} \\ H_x^{\ (1)+} e^{jk_z^{\ (1)+} z} & H_x^{\ (2)+} e^{jk_z^{\ (2)+} z} \end{bmatrix}$$

The 4x2 matrices $\underline{\underline{W}}^-(z), \underline{\underline{V}}^-(z)$ denote the negative modes.

(2.44)
$$\underline{\underline{W}}^-(z) = \begin{bmatrix} E_y^{\ (1)-} e^{jk_z^{\ (1)-} z} & E_y^{\ (2)-} e^{jk_z^{\ (2)-} z} \\ E_x^{\ (1)-} e^{jk_z^{\ (1)-} z} & E_x^{\ (2)-} e^{jk_z^{\ (2)-} z} \end{bmatrix}$$

(2.45)
$$\underline{\underline{V}}^-(z) = \begin{bmatrix} H_y^{\ (1)-} e^{jk_z^{\ (1)-} z} & H_y^{\ (2)-} e^{jk_z^{\ (2)-} z} \\ H_x^{\ (1)-} e^{jk_z^{\ (1)-} z} & H_x^{\ (2)-} e^{jk_z^{\ (2)-} z} \end{bmatrix}$$

The above equations can be expressed as below.

(2.46)
$$\begin{bmatrix} \underline{\underline{W}}_h & \underline{\underline{W}}_h \\ \underline{\underline{V}}_h & -\underline{\underline{V}}_h \end{bmatrix} \begin{bmatrix} \underline{\underline{\vec{U}}} \\ \underline{\underline{\vec{R}}} \end{bmatrix} = \begin{bmatrix} \underline{\underline{W}}^+(0) & \underline{\underline{W}}^-(z_- - z_+) \\ \underline{\underline{V}}^+(0) & \underline{\underline{V}}^-(z_- - z_+) \end{bmatrix} \begin{bmatrix} \underline{\underline{C}}_a^{\ +} \\ \underline{\underline{C}}_a^{\ -} \end{bmatrix}$$

(2.47)
$$\begin{bmatrix} \underline{\underline{W}}^{+}(z_{+}-z_{-}) & \underline{\underline{W}}^{-}(0) \\ \underline{\underline{V}}^{+}(z_{+}-z_{-}) & \underline{\underline{V}}^{-}(0) \end{bmatrix} \begin{bmatrix} \underline{\underline{C_a}}^{+} \\ \underline{\underline{C_a}}^{-} \end{bmatrix} = \begin{bmatrix} \underline{\underline{W_h}} & \underline{\underline{W_h}} \\ \underline{\underline{V_h}} & -\underline{\underline{V_h}} \end{bmatrix} \begin{bmatrix} \underline{\underline{\vec{T}}} \\ \underline{\underline{0}} \end{bmatrix}$$

The coupling coefficient matrix operators are obtained as below.

(2.48)

$$\begin{bmatrix} \underline{\underline{C_a}}^{+} \\ \underline{\underline{C_a}}^{-} \end{bmatrix} = \begin{bmatrix} \underline{\underline{W_h}}^{-1}\underline{\underline{W}}^{+}(0)+\underline{\underline{V_h}}^{-1}\underline{\underline{V}}^{+}(0) & \underline{\underline{W_h}}^{-1}\underline{\underline{W}}^{-}(z_{-}-z_{+})+\underline{\underline{V_h}}^{-1}\underline{\underline{V}}^{-}(z_{-}-z_{+}) \\ \underline{\underline{W_h}}^{-1}\underline{\underline{W}}^{+}(z_{+}-z_{-})-\underline{\underline{V_h}}^{-1}\underline{\underline{V}}^{+}(z_{+}-z_{-}) & \underline{\underline{W_h}}^{-1}\underline{\underline{W}}^{-}(0)-\underline{\underline{V_h}}^{-1}\underline{\underline{V}}^{-}(0) \end{bmatrix}^{-1} \begin{bmatrix} 2\underline{\underline{\vec{U}}} \\ \underline{\underline{0}} \end{bmatrix}$$

R and T are as given below.

(2.49)
$$\underline{\underline{\overleftarrow{R}}} = \underline{\underline{W_h}}^{-1}[\underline{\underline{W}}^{+}(0)\underline{\underline{C_a}}^{+} + \underline{\underline{W}}^{-}(z_{-}-z_{+})\underline{\underline{C_a}}^{-} - \underline{\underline{W_h}}\underline{\underline{\vec{U}}}]$$

(2.50)
$$\underline{\underline{\vec{T}}} = \underline{\underline{W_h}}^{-1}[\underline{\underline{W}}^{+}(z_{+}-z_{-})\underline{\underline{C_a}}^{+} + \underline{\underline{W}}^{-}(0)\underline{\underline{C_a}}^{-}]$$

The above analysis can be generalized to 2D and 3D medium. Here, 2D and 3D medium refer to material with a permittivity and permeability profile that varies in two dimensions and three dimensions. This generalized approach is referred to as the Fourier modal method and was applied in this research to visualize the electromagnetic characteristics for medium interfaces and to optimize the grating design required to implement the necessary diffractive efficiency.

Chapter 3. Diffractive optics for augmented reality

Chapter Overview

This chapter looks into the design of waveguide-based AR devices. The theoretical background employed for the specification of grating structure is explained. We briefly delve into the analysis of slanted gratings used for the design of the given waveguide and introduce how k-vector diagrams can be conveniently used to optimize the necessary grating parameters.

3.1. Analysis of slanted gratings using diffraction theory

Chevron gratings were assumed for the design of the waveguide within the scope of this dissertation[34837]. K-vector analysis is required to understand how Chevron gratings act to direct incident rays of light.

(2.51) $$\overrightarrow{K_{inc}} = (k_x, k_y, k_z) = \frac{2\pi}{\lambda}(\cos\varphi\sin\theta, \sin\varphi\cos\theta, \cos\theta)$$

(2.52) $$\overrightarrow{G} = (G_x, G_y, G_z) = \frac{2\pi}{\Lambda}(\cos\varphi_G \sin\theta_G, \sin\varphi_G \cos\theta_G, \cos\theta_G)$$

The k-vector of the incident ray and the grating vector can be expressed as the above. λ indicates the wavelength of light, whereas Λ refers to the grating period. The tangential k-vector component of the resulting ray after transmission or reflection is a sum of the tangential incident k-vector and the tangential grating vector multiplied by an integer. This integer m denotes the diffraction order. The perpendicular component of the resulting k-vector is decided by Eq. 3.3.

(2.53) $$k_x^{\ 2} + k_y^{\ 2} + k_z^{\ 2} = \frac{2\pi}{\lambda}$$

With a backward approach, it is possible to acquire the required grating vector for the light to be diffracted as intended. For instance,

in the below situation where light is incoupled into the waveguide, the following equations hold. The average refractive index considering the refractive indices of both media is denoted by n_{avg}.

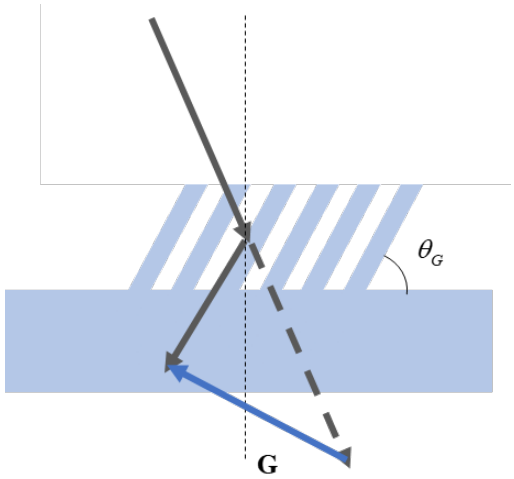

Fig. 438 A diagram of light incident to the input grating

$$\mathbf{k}_{inc} = \frac{2\pi}{\lambda} n(\sin\theta_{inc}, 0, \cos\theta_{inc}) = \frac{2\pi}{\lambda} n_{avg}(\sin\theta_{gr,inc}, 0, \cos\theta_{gr,inc})$$

(2.54) $$\mathbf{k}_{diff} = \frac{2\pi}{\lambda} n_{avg}(\sin\theta_{gr,diff}, 0, \cos\theta_{gr,diff}) = \mathbf{k}_{inc} + m\mathbf{G}$$

$$\mathbf{G} = \frac{2\pi}{\Lambda}(\sin\theta_G, 0, \cos\theta_G)$$

The above equations show the relations between grating vector $\mathbf{G}$ and incident and diffracted k−vectors k_{inc} and k_{diff}. It can be noted that depending on the desired angle of diffraction, the grating slanted angle $\theta_{\mathbf{G}}$ and grating period Λ can be varied accordingly.

3.2 K-vector diagram analysis for waveguide design

One of the drawbacks of waveguide-based AR glasses is that the TIR condition must be met for light to travel within the waveguide until it is outcoupled and directed towards the eye. This limitation imposes a constraint on the angle of light that can be coupled into the waveguide, resulting in an inherent limitation on the field of view for AR glasses[1].

Thus, it is necessary for the waveguide designer to keep in mind the TIR condition and to determine the appropriate grating parameters that maximize the field of view within feasible range. One convenient approach to visualize and analyze this process is by employing k-vector diagram analysis.

Since the k vector of the optical wave meets the below condition, when the k-vector is visualized in 3D space with the initial point of the vector at the origin, the end point will lie on a sphere of radius $\sqrt{\frac{2\pi}{\lambda}}n$.

(2.55) $$k_x^{\ 2} + k_y^{\ 2} + k_z^{\ 2} = \frac{2\pi}{\lambda}n^2$$

If the k-sphere and k-vector are orthogonally projected onto 2D coordinates so that the components orthogonal to the waveguide surface are eliminated, the endpoint of the orthogonally projected k-vector would lie on a circle of radius $\sqrt{\frac{2\pi}{\lambda}}n\sin\theta$ where θ is the incidence angle.

Due to the element of $\sin\theta$ introduced because of the orthogonal projection, Snell's law, as expressed below, would signify that when visualized in an orthogonally projected k-circle, the end point of k_1 and k_2 vectors would coincide.

(2.56) $$n_1 \sin\theta_1 = n_2 \sin\theta_2$$

The condition for total internal reflection, as expressed below, would signify that the total internal reflection condition is met if the end point of k_1 is outside the k-circle of radius $n_2\sqrt{2\pi/\lambda}$.

(2.57) $$n_1 \sin\theta_1 > n_2$$

The aforementioned factors combined with the fact that the diffracted k vector can simply be visualized as the vector sum of the incident k vector and the grating vector allows the use of k−vector diagrams as a convenient method to decide the grating vector requirements.

Chapter 4. Field of view expansion for augmented reality head-mounted display

Chapter Overview

We analyze a method to provide a horizontally wider field of view by employing double expanders. The concept of FOV is briefly explained. This is followed by an explanation of the geometric optics ray tracing simulation with MATLAB employed to model the double expander waveguide. We further elaborate on how the grating parameters were determined with k-vector analysis.

4.1. Field of View

Field of view has been a serious issue for AR devices. Waveguide-based AR devices enforce total internal reflection requirements to the incoupled light for the rays to travel across the waveguide[5]. Due to the fact that the real-world imagery must be transmitted through the waveguide, transparency issues eliminate the possible use of waveguides with high-refractive indices that would relax TIR-related constraints. The method modeled in this dissertation is fundamentally a spatial multiplexing scheme by which portions of the image are delivered to the eye via different passageways.

4.2. Dual expander design for wider field of view

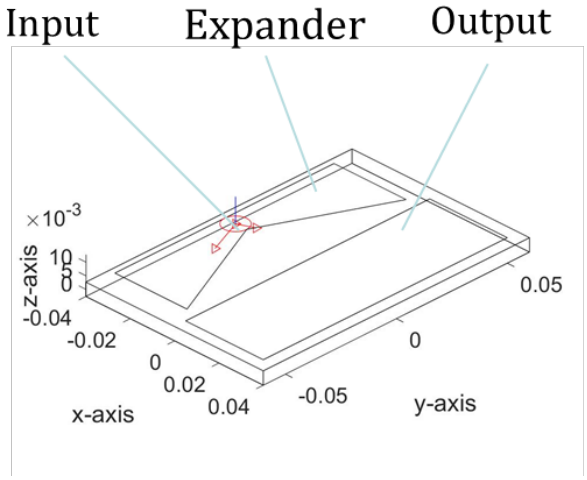

Fig. 4.2 Geometric optics modeling of dual expander waveguide design

Fig. 4.2 represents a diagram of a dual expander waveguide as modeled with geometric optics. This is based on the likely modeling of the HoloLens 2 optical combiner by Microsoft[6]. The waveguide consists of three individual regions as indicated: input, expander, and output. The expander consists of two different portions, referred to as the "left wing" and "right wing" for convenience. A portion of light from the image is spatially multiplexed to either the left or the right wing. Unlike the expander, the output region is a combined area. The three different regions act to couple the incoming light into the waveguide, multiply the optical rays, and to outcouple the light and to direct it to the user's eye.

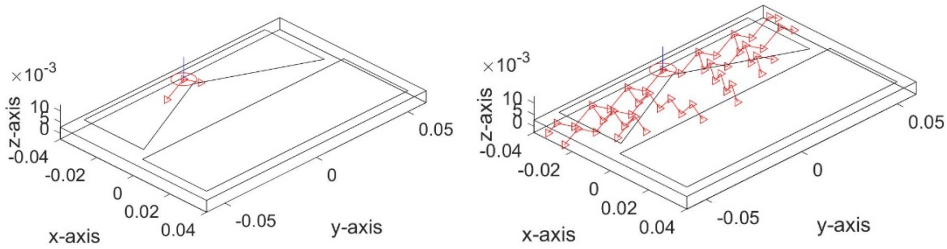

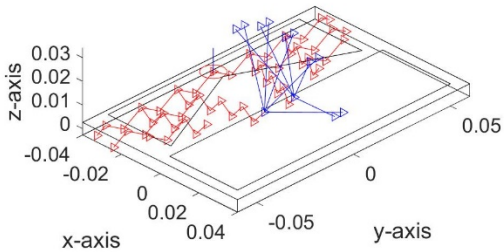

Fig. 4.3 Ray tracing simulation results for dual expander waveguide

Fig. 4.3 is a demonstration of the ray tracing simulation results for the given waveguide. MATLAB was used for the simulation. After the overall structure of a dual expander waveguide was decided, the four regions (input, left wing expander, right wing expander, and output) were each assigned a different grating vector according to the k-vector analysis that will be elaborated in the next section.

When an image is loaded into the program, the ray tracing starts at each pixel point. In terms of the program, when a "ray" meets a new surface, the prior ray information is saved as Mom_ray and the resulting rays are considered to be the next generation of rays and their information is saved to child_ray. Each generation indicates an expansion of the tree data structure until the ray meets certain conditions which indicate that the ray has gone beyond the limits of the structure. After this is finished for a single ray starting at the image pixel point, the above process is repeated for the next ray starting at a different image pixel.

After the first generation ray meets the input grating surface, the k-vector of the ray is altered by the input grating vector so that according to the +1 and −1 diffraction order, the rays each enter the left and right wing expander regions. In the left and right wing expander regions, the grating vectors of the grating surfaces are each given so that a 1st order diffraction will lead to the ray acquiring a directional component towards the output region. For a zeroth order diffraction, rays will continue on in the y-axis direction. Through this process, the eye box is expanded in the horizontal dimension and are directed towards the expander region. Finally, in the expander region, the rays in the expander region are

coupled outwards according to the order of diffraction. Zeroth order diffraction leads to some rays continuing on in the downward direction, leading to an eye box expansion in the vertical direction.

4.3. Grating design with k−vector analysis

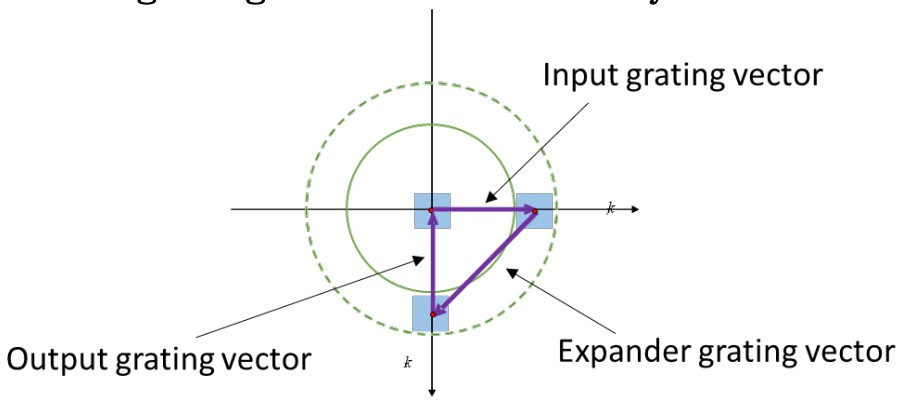

Fig. 4.4 K−vector diagram for a single expander AR waveguide

An example of a k−vector diagram orthogonally projected onto the $k_x - k_y$ plane is shown in Fig. 4.4. The k−vector of a light ray orthogonally projected into the input grating region of the waveguide is represented as a red dot at the origin since it has no tangential components. The blue rectangle surrounding the red point indicates the field of view.

Due to the input grating vector indicated as a purple arrow in Fig. 4.4, the optical wave vector corresponding to the red point at the origin would be altered to point towards the red dot when orthogonally projected. More specifically, the resultant diffracted vector would be a sum of the input grating vector and the incident wave vector and would end at a point on the sphere of radius $n_2\sqrt{2\pi/\lambda}$, where n_2 is the refractive index of the waveguide. That end point, when projected onto the $k_x - k_y$ plane would coincide with the red point at the end of the input grating vector as indicated in the diagram.

Optical wave vectors that are incident to the input grating at a nonzero angle are also diffracted in a similar manner. It may be noted, however, that for the diffracted k−vector to meet TIR requirements, the endpoint of the diffracted k−vector, when orthogonally projected onto the $k_x - k_y$ plane must exist between the two k−circles of radius $n_1\sqrt{2\pi/\lambda}$ and $n_2\sqrt{2\pi/\lambda}$.

The expander grating vector is then added to the diffracted k−

vector, redirecting it towards a different point on the sphere of radius $n_2\sqrt{2\pi/\lambda}$. Again, the diffracted k−vector must also meet the TIR conditions, thus limiting the field of view to the blue rectangle indicated. Finally, the output grating vector is added to the optical wave vector, and the diffracted wave vector corresponds to a vector pointing towards the eye, with diminished tangential components. The diffracted wave vector would end at a point on the sphere of radius $n_1\sqrt{2\pi/\lambda}$.

To achieve a broader field of view, it is necessary to enlarge the area of the blue rectangle that satisfies the TIR condition. The necessary grating vectors can be calculated with this diagram alone. The grating vectors assigned to each region−incoupler, expander, and outcoupler−was as noted below.

$$\mathbf{G}_i = (0, -1.0375k_0, 0.7875k_0)$$
$$\mathbf{G}_e = (1.3038k_0, -1.3038k_0, 0)$$
$$\mathbf{G}_i = (1,2796k_0, 0, 0)$$

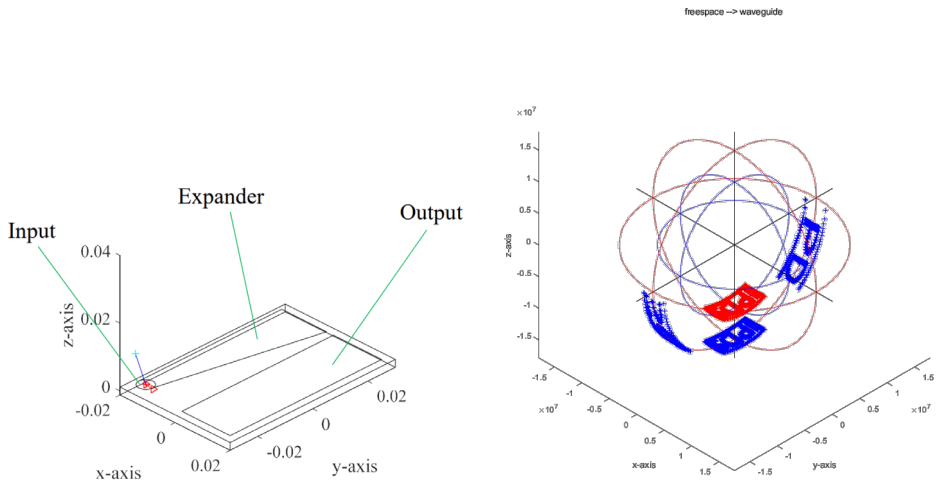

Fig. 4.5 The ray tracing simulations for a single expander waveguide and the corresponding k−vector diagram: input grating

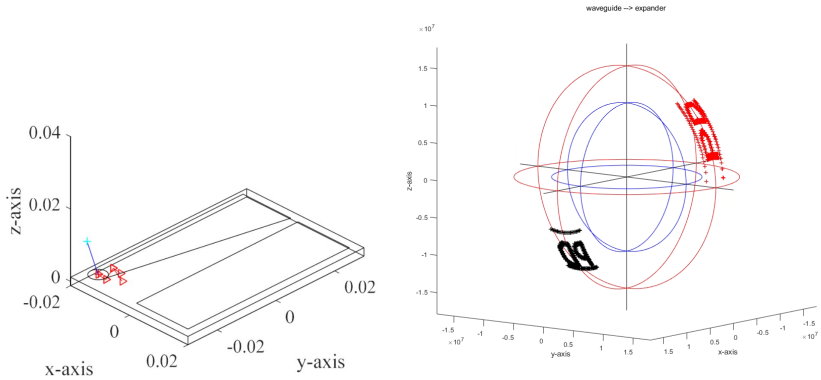

Fig. 4.6 The ray tracing simulations for a single expander waveguide and the corresponding k−vector diagram: expander grating

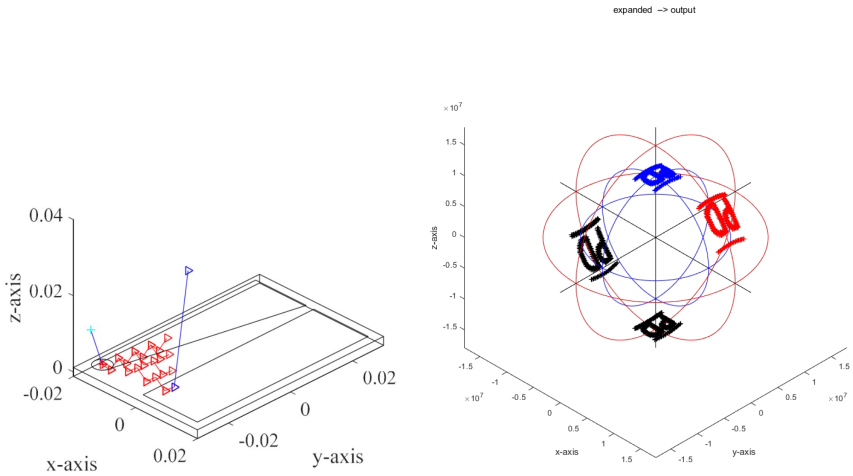

Fig. 4.7 The ray tracing simulations for a single expander waveguide and the corresponding k−vector diagram: output grating

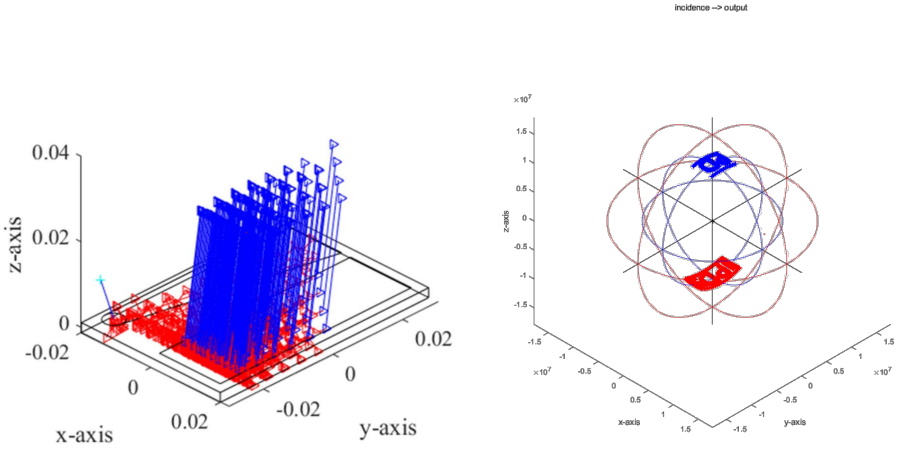

Fig. 4.8 The ray tracing simulations for a single expander waveguide and the corresponding k−vector diagram. The k−vector

diagram indicates the incoupled and outcoupled wave vector.

For a dual expander waveguide, the k-vector diagram takes on a different form, consequently leading to an improved FOV.

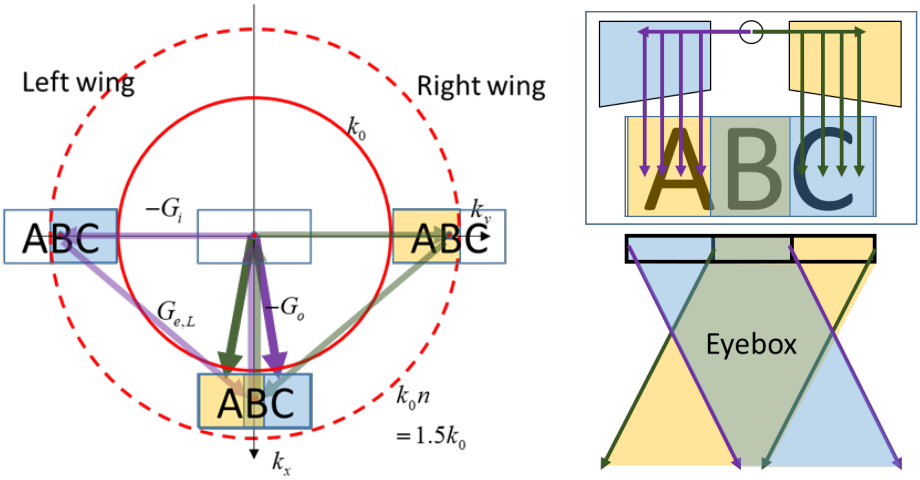

Fig. 4.8 The k-vector diagram for a dual expander waveguide

Fig. 4.8 is the k-vector diagram for a dual expander waveguide. The horizontal width of the field of view has significantly been enlarged. If the image of letters ABC are to be projected to the user, optical waves corresponding to AB are expanded through the right wing, whereas BC are expanded through the left. The wavevectors corresponding to A in the left wing and the C in the right wing are not delivered to the user, as they are out of bounds when it comes to the condition that the k-vector end point must exist on the surface of the sphere of radius $n_2\sqrt{2\pi/\lambda}$.

The waveguide is designed so that BC, not AB, are expanded by the left wing. This is because when the angle of the light finally outcoupled is considered, a wider overlapping region to perceive the light from the left and right wing is advantageous. This overlapping region would be where all three alphabets would be perceived and thus, the eye box.

The grating vectors assigned to each region-incoupler, right wing expander, left wing expander, and outcoupler-was as below.

$$\mathbf{G}_i = (0, -1.3025k_0, 0)$$
$$\mathbf{G}_{e,R} = (0.9219k_0, -1.5968k_0, 0)$$
$$\mathbf{G}_{e,R} = (0.9219k_0, 1.5968k_0, 0)$$
$$\mathbf{G}_i = (0.3836k_0, 0, 0)$$

4.4. Wire Grid Polarizer for full-color operation

Full color operation with a single waveguide while maintaining a large FOV is also a main challenge. As light waves differ in wavelength, naturally, k-vectors differ. Below is the k-vector diagram for full-color operation of the suggested waveguide.

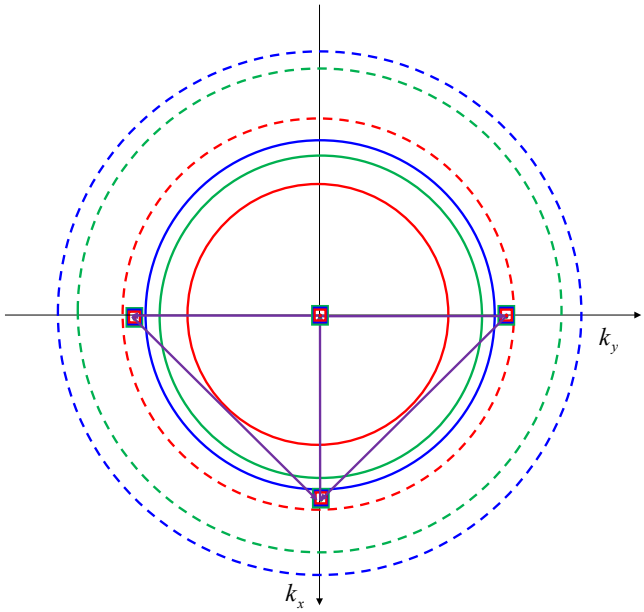

Fig. 4.9 K-vector diagram for the full-color operation of the dual expander waveguide

The wavelengths of red, green, and blue were assigned as follows.

$$\lambda_R = 633nm, k_{R,0} = \frac{2\pi}{\lambda_R}$$

$$\lambda_G = 512nm, k_{G,0} = \frac{2\pi}{\lambda_G} = k_{R,0}\frac{\lambda_R}{\lambda_G} = 1.2363k_{R,0}$$

$$\lambda_G = 473nm, k_{B,0} = \frac{2\pi}{\lambda_B} = k_{R,0}\frac{\lambda_R}{\lambda_G} = 1.3383k_{R,0}$$

Due to the differences in k-vectors the field of view for which images of all three colors can be perceived by the user is seriously limited and is smaller than 10.2 degrees according to calculation.

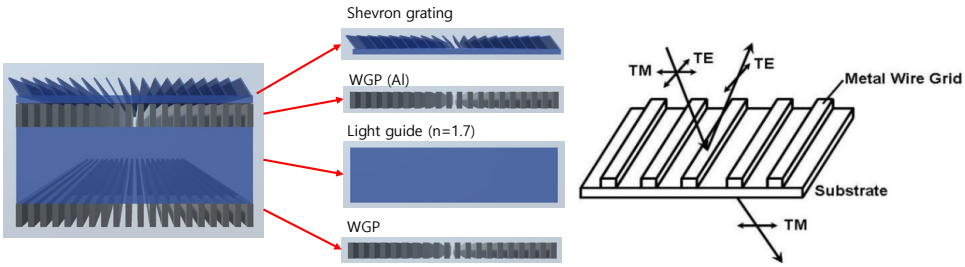

Fig. 4.10 Wire grid polarizers with waveguide AR

Wire grid polarizers offer a promising solution to address the constraint of waveguide-based AR devices caused by total internal reflection (TIR) conditions. These polarizers selectively reflect or transmit nearly all incident light that is polarized in the transverse electric (TE) or transverse magnetic (TM) orientation. By relaxing the strict requirements of TIR, the field of view (FOV) of such devices can be enlarged, allowing for improved full-color operation.

Wire grid polarizers consist of parallel metal wires oriented in a certain direction. The underlying principle is that for TE-polarized light, the electric field is oriented parallel to the metal wires, which excites electrons along the wires. As a result, the wire grid polarizer behaves similarly to a typical metal surface, leading to complete reflection of TE-polarized light. On the other hand, TM-polarized waves, with the electric field perpendicular to the wires, are mostly transmitted[7].

By incorporating wire grid polarizers into waveguide-based AR devices, the FOV can be expanded by allowing a larger range of light to traverse within the waveguide with high reflection even though under typical circumstances, the angle of incident light would not allow total internal reflection.

The relaxation of the TIR conditions effectively allows for a significantly larger FOV. Simulations were performed by loading an image corresponding to a FOV of 90 degrees. The key observation is that wave vectors that would have otherwise failed to meet the TIR requirements are internally reflected across the waveguide, thus allowing the possibility for these wave vectors to be ultimately outcoupled.

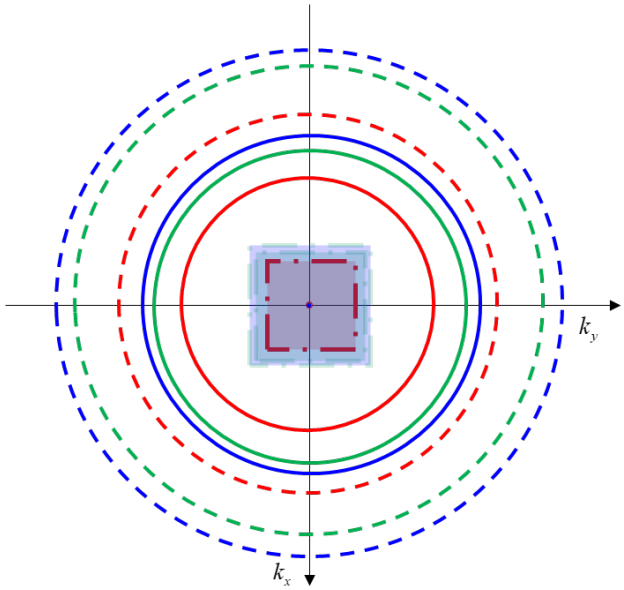

Fig. 4.11 K-vector diagram for the full-color operation of a double expander waveguide with WGP

Simulations were performed by loading an image corresponding to a FOV of 90 degrees. Because of the difference in the magnitude of the k-vector corresponding to different optical wavelengths, the results of higher order diffraction for blue and green are visible on the k-diagram for the incoupler. On the other hand, the second order diffraction of the color red(633nm) does not meet requirements.

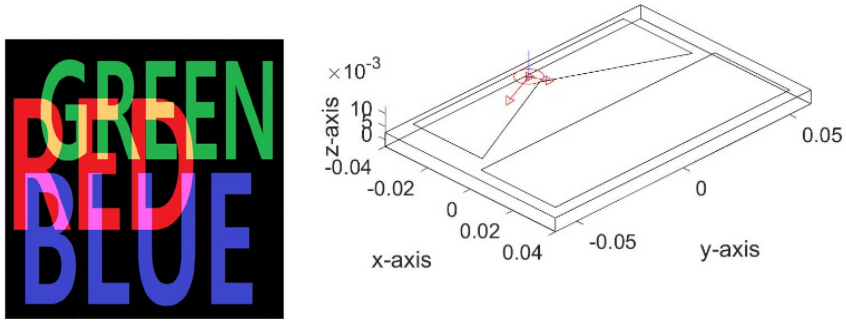

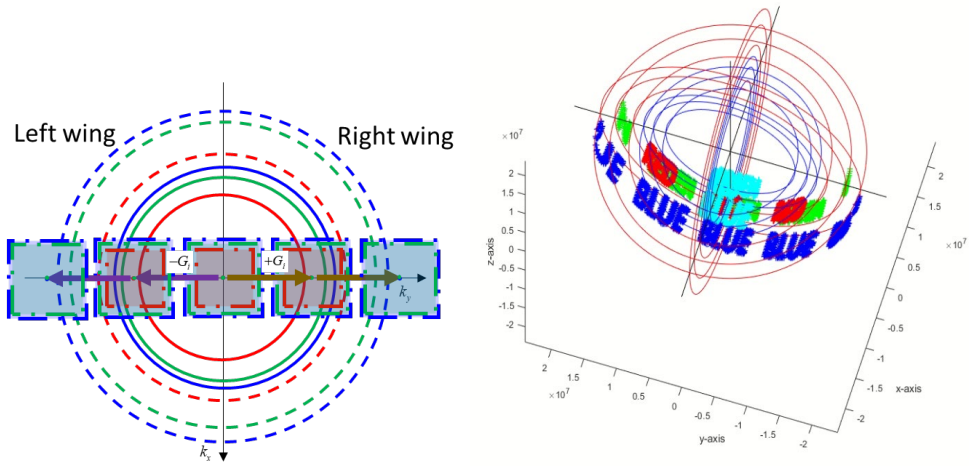

Fig. 4.12 K−vector diagram for the full−color operation of a double expander waveguide with WGP: incoupler grating

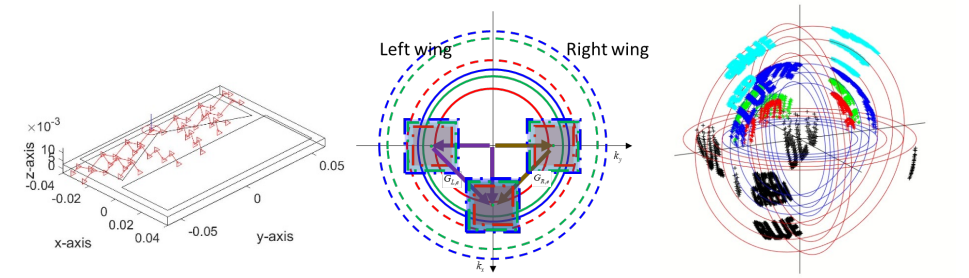

Fig. 4.13 K−vector diagram for the full−color operation of a double expander waveguide with WGP: expander grating

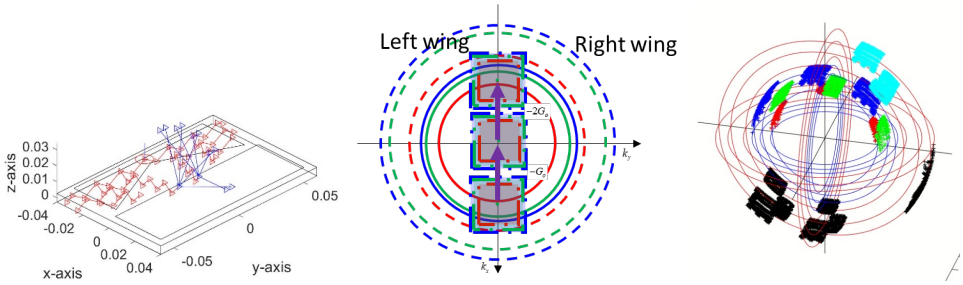

Fig. 4.14 K−vector diagram for the full−color operation of a double expander waveguide with WGP: outcoupler

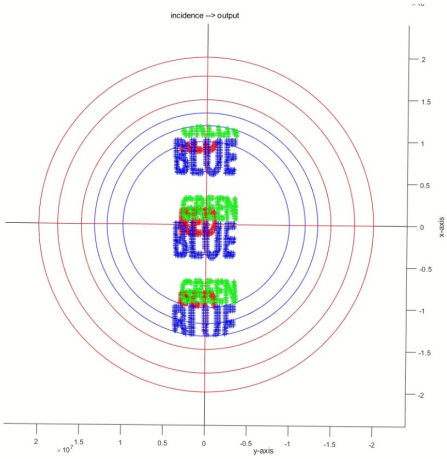

Fig. 4.15 K-vector diagram of the resultant outcoupled wavevectors for the full-color operation of a double expander waveguide with WGP

Chapter 5. Eye box expansion for augmented reality head-mounted display

Chapter Overview

In this chapter, we present methods of eye box expansion for waveguide-based AR display. The common objective of the presented methods is to integrate the expander and output area so that a larger portion of the waveguide may outcouple light. Two methods are investigated: overlaid gratings and rhombus-shaped gratings. Frustrated total internal reflection is explained to understand the working principle of overlaid gratings. Methods for optimizing diffraction efficiency for a uniform output in expander-outcoupler integrated waveguides is presented.

5.1. Eye Box

In augmented reality displays, the eye box refers to an area or volume of space within which the user's eye must be positioned to perceive the virtual imagery provided by the HMD[8, 9]. A larger eye box permits more user freedom in eye positioning and head movement with minimal aberrations or misalignment issues. In order to improve the eye box, there are attempts to integrate the expander and outcoupler into a single grating region that both expands the eye box in two dimensions as well as outcouples the light towards the user's eye.

5.2. Frustrated Total Internal Reflection

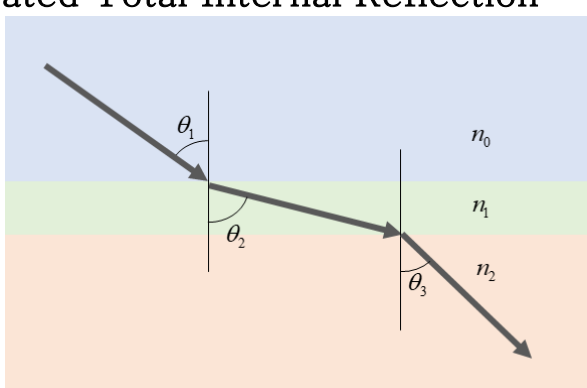

Fig. 5.1 A diagram depicting frustrated total internal reflection

Frustrated total internal reflection (FTIR) refers to the phenomenon where light is partially transmitted at an interface although the incident angle satisfies the total internal reflection condition. This occurs when there is a nanoscale gap between the first medium and the second medium at the interface of light incidence[10].

By stacking two different grating structures, FTIR can be used to allow a portion of incident light to be affected by both grating vectors, opening the possibility for a combined grating structure that acts as both a two-dimensional exit pupil expander and an output grating. To elaborate, the grating nearer to the waveguide would perform to multiply the rays across two dimensions and to act as the exit pupil expander. However, as there is a nanometer gap between the two gratings at the interface, a portion of the light that satisfies TIR conditions will be transmitted and interact with the superimposed grating. The second grating structure would act as the output grating[11].

The application of this method of grating design and the surface relief gratings as seen in the WaveOptics patent mentioned in Section 5.3 would lead to the two different light outcoupling pattern as demonstrated in Fig. 5.3.

5.3. Integrated expander and outcoupler design

The modeling of a waveguide with expander and outcoupler integration is presented based on rhombus-shaped surface relief gratings as seen in a WaveOptics patent[12].

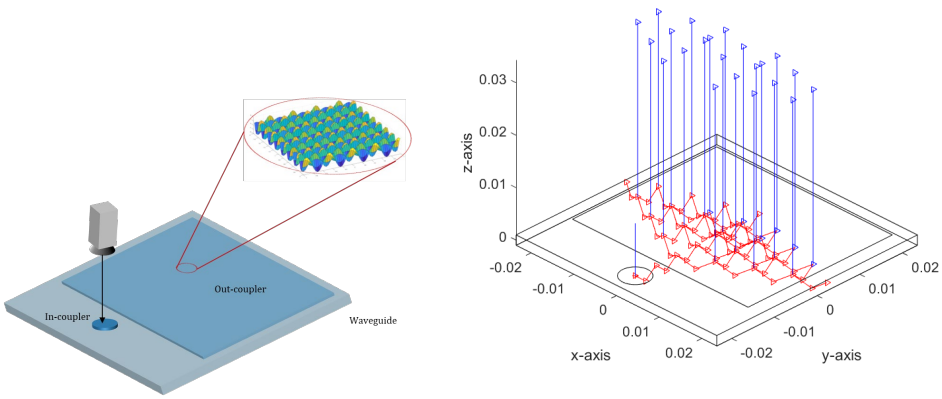

Fig. 5.2 Diagram of an integrated expander-outcoupler waveguide and the demonstration of a ray tracing simulation

Geometric optics modeling and simulation techniques were used

along with k-vector analysis to attain the necessary grating vectors for the appropriate performance of the integrated expander-outcoupler waveguide.

As can be observed from Fig. 5.2, a single region of grating acts as both the expander and the outcoupler. Portions of the light rays are outcoupled while the remainder continue to traverse the waveguide while multiplying in two dimensions.

5.4. Diffraction efficiency encoding for uniform output

A spatial-division diffraction efficiency encoding was performed for the integrated diffractive waveguide combiner to improve the uniformity of the outcoupled light.

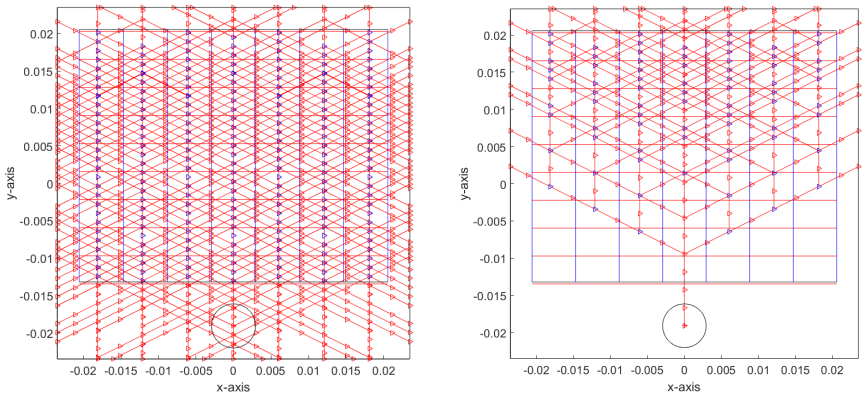

Fig. 5.3 A bird's eye view of the ray tracing results of two expander-outcoupler integrated waveguides

The above figure demonstrates the ray tracing results of two waveguides. For the one on the left, higher order diffraction was considered, whereas the simulation on the right assumed diffraction limited to the first order. As the points where outcoupling occurs are distinct, especially for case b, the region of outcoupling was partitioned into 63 regions of interest for the optimization of the diffraction efficiency for uniform areal light outcoupling.

The cost function was defined as the variance of wave energy

across the 63 sectioned regions. $\bar{E}$ denotes the average value for all 63 zones. The zone numbers are indicated with m and n.

$$\sigma^2 = \frac{\sum_{m,n}(E_{m,n} - \bar{E})^2}{mn} \tag{2.58}$$

Genetic algorithm was utilized to minimize the above defined variance. The structure of the genetic algorithm is as shown below.

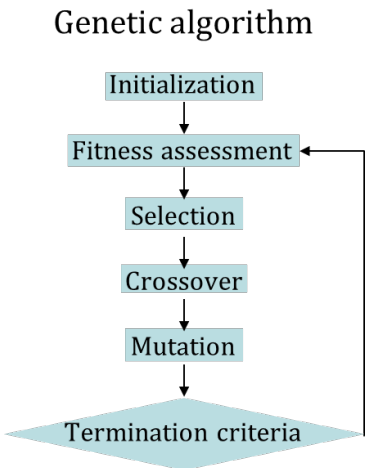

Fig. 5.4 Diagram for a genetic algorithm

Genetic algorithms, in general, are a type of metaheuristic algorithm inspired by the evolutionary process in nature. A population is first initialized, and these "chromosomes" are evaluated. Based on the evaluation results, a number of chromosomes are selected. During crossover, random chromosomes are chosen from the pool of chromosomes that have undergone selection, and portions of the chromosomes are interchanged randomly. Mutation adds an additional element of randomness by changing the chromosome information based on probability [13].

For the task assigned in this dissertation, a population size of twenty was selected, with the variable count being 144 for case a and 84 for case b.

After the genetic algorithm, the results were post processed so that the diffraction efficiencies were modified in a row-by-row manner. This step was especially effective for case b for which the

light rays cannot return to a previous row, but must either be outcoupled or continue downwards.

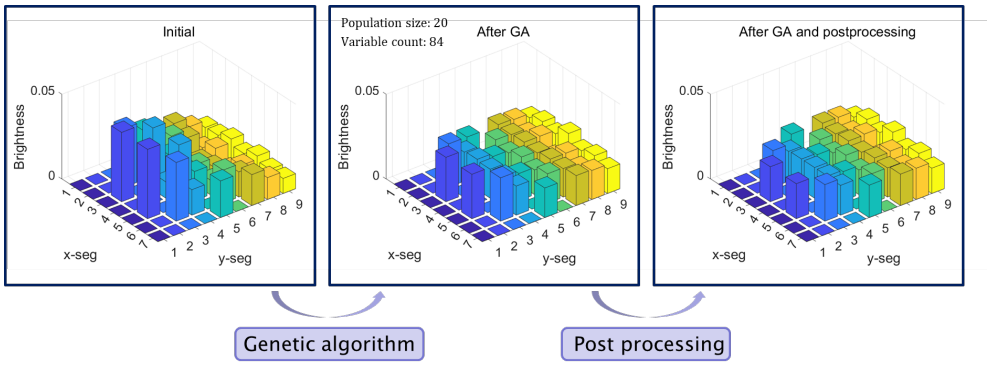

Fig. 5.5 Diffraction efficiency optimization results for case b waveguide combiner

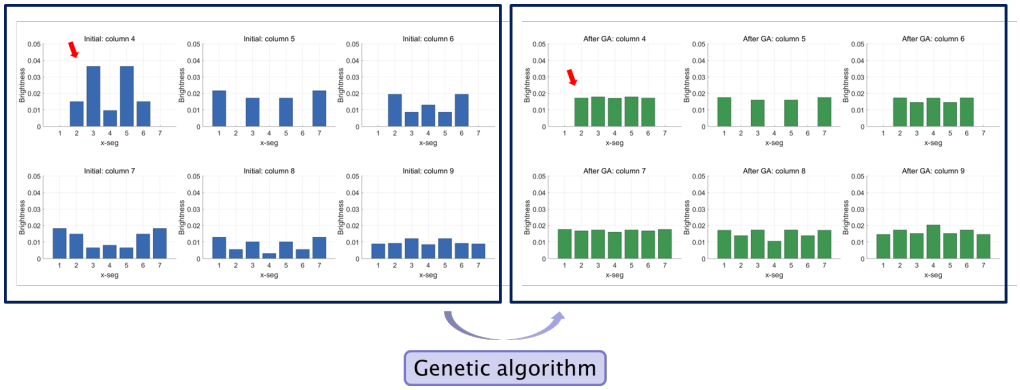

Fig. 5.6 A row-by-row view of how the uniformity of the outcoupling light was improved with the use of genetic algorithm for case b

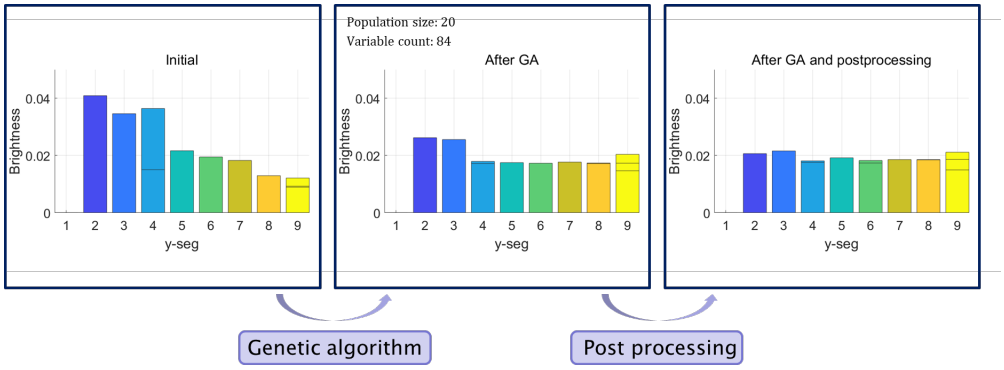

Fig. 5.7 A column view of the uniformity distribution after genetic algorithm and post processing for case b

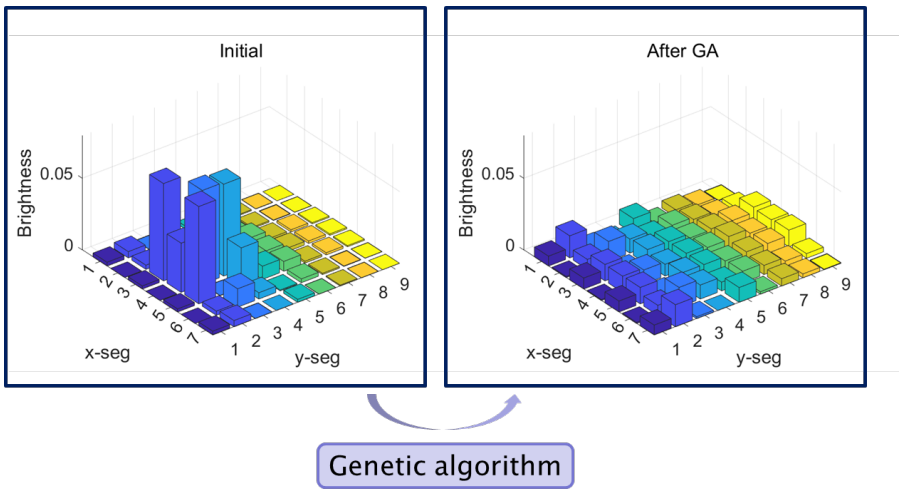

Fig. 5.8 The uniformity distribution after genetic algorithm for case a

Chapter 6. Conclusion

In this dissertation, we analyzed the waveguide optical combiner for AR NED devices. The focus of this research was to endeavor to address the issues of limited field of view and eye box. The presented waveguide models were validated with a geometric-optics ray tracing system, and the design of the diffractive optical elements was performed with k-vector analysis.

The diffractive optical element chosen to alter the optical wavevector was Chevron gratings and rhombus shaped surface relief gratings. Based on the required grating vectors as calculated with k-vector analysis, the parameters for the Chevron gratings were attained, including grating period and angle.

Models were presented for improved field of view and eye box. Enhancement of the horizontal field of view was suggested with the use of spatial multiplexing through dual expanders. This model was validated with both ray-tracing and k-vector diagram simulation. The grating vectors were assigned so that the light from the image portion expanded through the left wing would actually be the right side of the image. This intercross was designed to maximize the eye box for the dual expander waveguide. Further research may be conducted with spatial multiplexing across three or more waveguides that are each tilted at different angles so that the system resembles a curved waveguide. Additional approaches for a curved waveguide will be investigated.

The issue of the eye box was addressed by attempting to integrate the expander and the outcoupler so that a larger area can outcouple light. Frustrated total internal reflection could be a viable option by superimposing two different gratings, with a portion of light being transmitted to the second grating and being ultimately outcoupled. Rhombus-shaped surface relief gratings were also investigated. Under more generalized, theoretical circumstances, optimal spatial-division diffraction efficiency encoding was

presented with the objective of uniform areal light outcoupling. The optimization process was conducted with genetic algorithm and a post-processing step.

AR devices still face various challenges that are hindering its wide commercialization. For a genuinely immersive user experience, the quality of the display is key. We hope that the results of this dissertation offer a means to come closer to overcoming the limitations that current AR devices possess.

Bibliography

[1] J. Xiong, E.-L. Hsiang, Z. He, T. Zhan, and S.-T. Wu, "Augmented reality and virtual reality displays: Emerging technologies and future perspectives", *Light: Science & Applications*, vol. 10, no.1, 2021.

[2] J. Carmigniani *et al.*, "Augmented reality technologies, systems and applications", *Multimedia tools and applications*, vol. 51, pp. 341-377, 2011.

[3] H. Kim, J. Park, and B. Lee, *Fourier modal method and its applications in computational nanophotonics*. CRC Press, 2017.

[4] A. Babaeihaselghobi *et al.* "A novel chevron-shape double-staggered grating waveguide slow wave structure for terahertz traveling wave tubes." *IEEE Transactions on Electron Devices* vol. 67, no. 9, pp. 3781-3787, 2020.

[5] B. Kress, "Optics for smart glasses, smart eyewear, augmented reality and virtual reality headsets," *Fundamentals of Wearable Computers and Augmented Reality, Second Edition*, W. Barfield, 2015.

[6] B. C. Kress and W. J. Cummings, "Towards the ultimate mixed reality experience: HoloLens display architecture choices," *Dig. Tech. Pap. - Soc. Inf. Disp. Int. Symp.,* vol. 48, no. 1, pp. 127-131, 2017.

[7] X. J. Yu, and H. S. Kwok, "Optical wire-grid polarizers at oblique angles of incidence." *Journal of Applied Physics*, vol. 93, no. 8, pp. 4407-4412, 2003.

[8] Steven A. Cholewiak, Zeynep Başgöze, Ozan Cakmakci, David M. Hoffman, and Emily A. Cooper, "A perceptual eyebox for near-eye displays," *Opt. Express*, vol. 28, pp. 38008-38028, 2020.

[9] O. Cakmakci, D. M. Hoffman, and N. Balram, "3D eyebox in augmented and virtual reality optics," *SID Symposium Digest of Technical Papers*, vol. 50, pp. 438-441, 2019.

[10] S. Zhu *et al.*, "Frustrated total internal reflection: A demonstration and review." *American Journal of Physics,* vol. 54, no. 7, pp. 601-607, 1986.

[11] J. Choi *et al.* "Numerical design and analysis of diffractive optic AR glass." Master dissertation, College of Eng., Korea Univ., Sejong, 2019.
[12] D. J. Grey and M. S. Valera, "Waveguide for an augmented reality or virtual reality display," Patent 2018178626, Mar. 16, 2018.
[13] M. Kumar *et al.* "Genetic algorithm: Review and application", *Available at SSRN 3529843*, 2010.

초 록

증강현실 (AR: Augmented Reality) 근안 디스플레이 (NED: Near-Eye Display) 시스템은 이용자의 실제 주변 이미지에 가상 이미지가 중첩되어 이용자 눈에 도달하게 함으로써 실제 세상에 대한 경험을 향상시키고자 한다. 지난 몇 년 간 이 분야에 대한 관심은 극대화되었으며, 몰입도 있는 메타버스 경험을 위한 헤드 마운트 디스플레이에 대한 수요도 나날이 증가하고 있다. 하지만 다양한 발전에도 불구하고 여러 가지 도전이 남아 있다.

AR NED 시스템은 밝기나 픽셀 품질 등 전통적인 디스플레이 관련 문제뿐 아니라 근안 디스플레이 특유의 도전 과제 또한 당면하고 있다. 예를 들어, field of view (FOV)와 eye box(EB)는 디스플레이 시스템과 눈의 근접성 때문에 부각되는 디스플레이 품질 요소로, 이에 대한 연구가 활발히 진행되고 있다.

본 논문에서는 AR NED 시스템의 FOV와 EB를 개선하는 것을 주요 목표로 설정한다. 기하 광학 기반의 광선 추적과 k-벡터 분석, 그리고 Fourier modal method (FMM)을 이용하여 제시된 광도파로 모델의 설계와 검증을 수행한다. FOV 확장을 위해 광선다발 복제/확장 역할의 광도파로가 이중으로 설계된 광도파로를 분석한다. EB 개선을 위해 광선 다발을 복제/확장하는 광도파로 구조와 눈의 방향으로 출력시키는 구조가 결합된 광도파로를 설계, 분석한다. 이 광도파로의 균일한 광 출력을 위해 유전 알고리즘과 추가적인 후처리 단계를 통해 회절 효율 최적화를 한다.

주요어 : 증강 현실, 회절 광학, 근안 디스플레이, 헤드 마운트 디스플레이, 광선 추적, Fourier modal method
학번 : 2021-20673